DSS-24 Microwave Holography Measurements

D. J. Rochblatt, P. M. Withington, and H. J. Jackson
Ground Antennas and Facilities Engineering Section

The JPL DSN Microwave Antenna Holography System (MAHST) was applied to the newly constructed DSS-24 34-m beam-waveguide antenna at Goldstone, California. The application of MAHST measurements and corrections at DSS 24 provided the critical RF performance necessary to not only meet the project requirements and goals, but to surpass them. A performance increase of 0.35 dB at X-band (8.45 GHz) and 4.9 dB at Ka-band (32 GHz) was provided by MAHST, resulting in peak efficiencies of 75.25 percent at X-band and 60.6 percent at Ka-band (measured from the Cassegrain focus at f1). The MAHST enabled setting the main reflector panels of DSS 24 to 0.25-mm rms, making DSS 24 the highest precision antenna in the NASA/JPL DSN. The precision of the DSS-24 antenna (diameter/rms) is 1.36×10^5, and its gain limit is at 95 GHz.

I. Introduction

The JPL Microwave Antenna Holography System (MAHST) (Fig. 1) [1] has become the leading technique for increasing the performance of the large NASA/JPL DSN antennas, especially at the shorter wavelengths (X-band (8.45 GHz) and Ka-band (32 GHz)). The MAHST provides an efficient and low-cost technique to optimize and maintain the performance and operation of the large DSN antennas, providing far-field amplitude and phase pattern measurement with a 90-dB dynamic range, and enabling high-resolution and high-precision antenna imaging with a standard deviation of 100 μm. The panel setting/unbending screw adjustment is provided with an accuracy of 10 to 20 μm. Fast subreflector position optimization is provided, which increases the antenna performance capacity and pointing accuracy. The MAHST is a portable system that can be shipped to any DSN antenna around the world and can be easily interfaced with its encoders and antenna drive systems. The MAHST was designed utilizing many off-the-shelf commercially available components. The remaining parts were designed and built at JPL. The MAHST has been successfully tested and demonstrated at the NASA/JPL DSN [1,2].

The microwave holography technique utilizes the Fourier transform relationship between the complex far-field radiation pattern of an antenna and the complex aperture field distribution. Resulting aperture phase and amplitude distribution data are used to derive various crucial performance parameters, including panel alignment, subreflector position, antenna aperture illumination, directivity at various frequencies, and gravity deformation effects [3,4]. Strong continuous wave (CW) signals obtained from geostationary satellite beacons are utilized as far-field sources. Strong CW beacon signals are available on nearly all satellites at Ku-band (10.7 to 12.7 GHz), X-band (7.0 to 7.8 GHz), and C-band (3.7 to 4.2 GHz). A portable 2.8-m reference antenna (Fig. 1) is used as a phase reference and provides the signal to the receiver phase-lock-loop (PLL) channel. The intermediate-frequency (IF) section of a Hewlett Packard Microwave Receiver (HP8530A) and an external JPL-designed and -built PLL enable
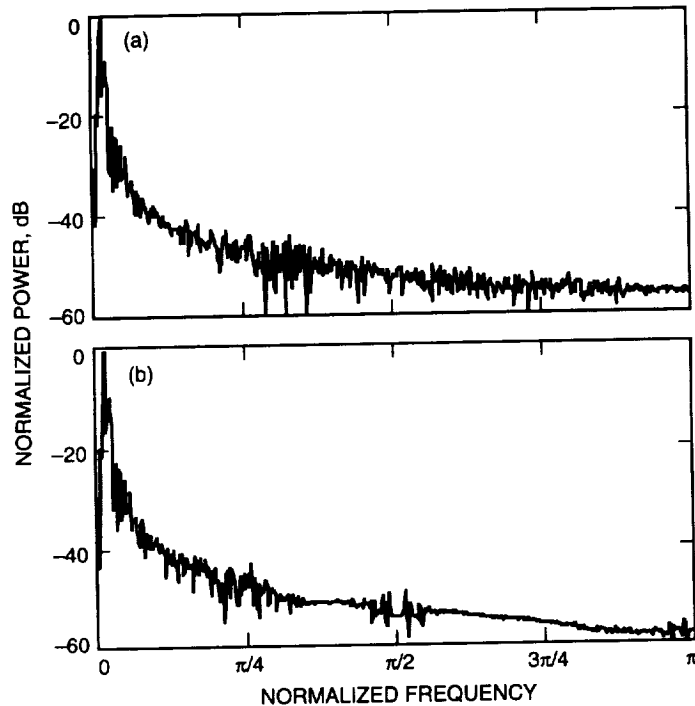
Fig. 12. Periodograms of 1024-point BHZ (20 samples/s) background (i.e., nonevent) data constructed from (a) the original and (b) the reconstructed waveform with low-resolution quantizer.

References

[1] A. N. Akansu and R. A. Haddad, *Multiresolution Signal Processing*, San Diego California: Academic Press, 1992.

[2] A. B. Kiely, "Bit-Wise Arithmetic Coding for Data Compression," *The Telecommunications and Data Acquisition Progress Report 42-117, January–March 1994*, Jet Propulsion Laboratory, Pasadena, California, pp. 145–160, May 15, 1994.

[3] R. J. McEliece and T. H. Palmatier, "Estimating the Size of Huffman Code Preambles," *The Telecommunications and Data Acquisition Progress Report 42-114, April–June 1993*, Jet Propulsion Laboratory, Pasadena, California, pp. 90–95, August 15, 1993.

[4] A. V. Oppenheim and R. W. Schafer, *Digital Signal Processing*, Englewood Cliffs, New Jersey: Prentice-Hall, 1975.

[5] M. Rabbani and P. W. Jones, *Digital Image Compression Techniques*, Bellingham, Washington: SPIE Press, 1991.

[6] A. S. Spanias, S. B. Jonsson, and S. D. Stearns, "Transform Methods for Seismic Data Compression," *IEEE Trans. Geoscience and Remote Sensing*, vol. 29, no. 3, pp. 407–416, May 1991.

[7] P. P. Vaidyanathan, *Multirate Systems and Filter Banks*, Englewood Cliffs, New Jersey: PTR Prentice-Hall, 1993.

[8] *Workshop on the Use of Data Compression in Seismic Data Proceedings*, Jet Propulsion Laboratory, Pasadena, California, March 2, 1994.
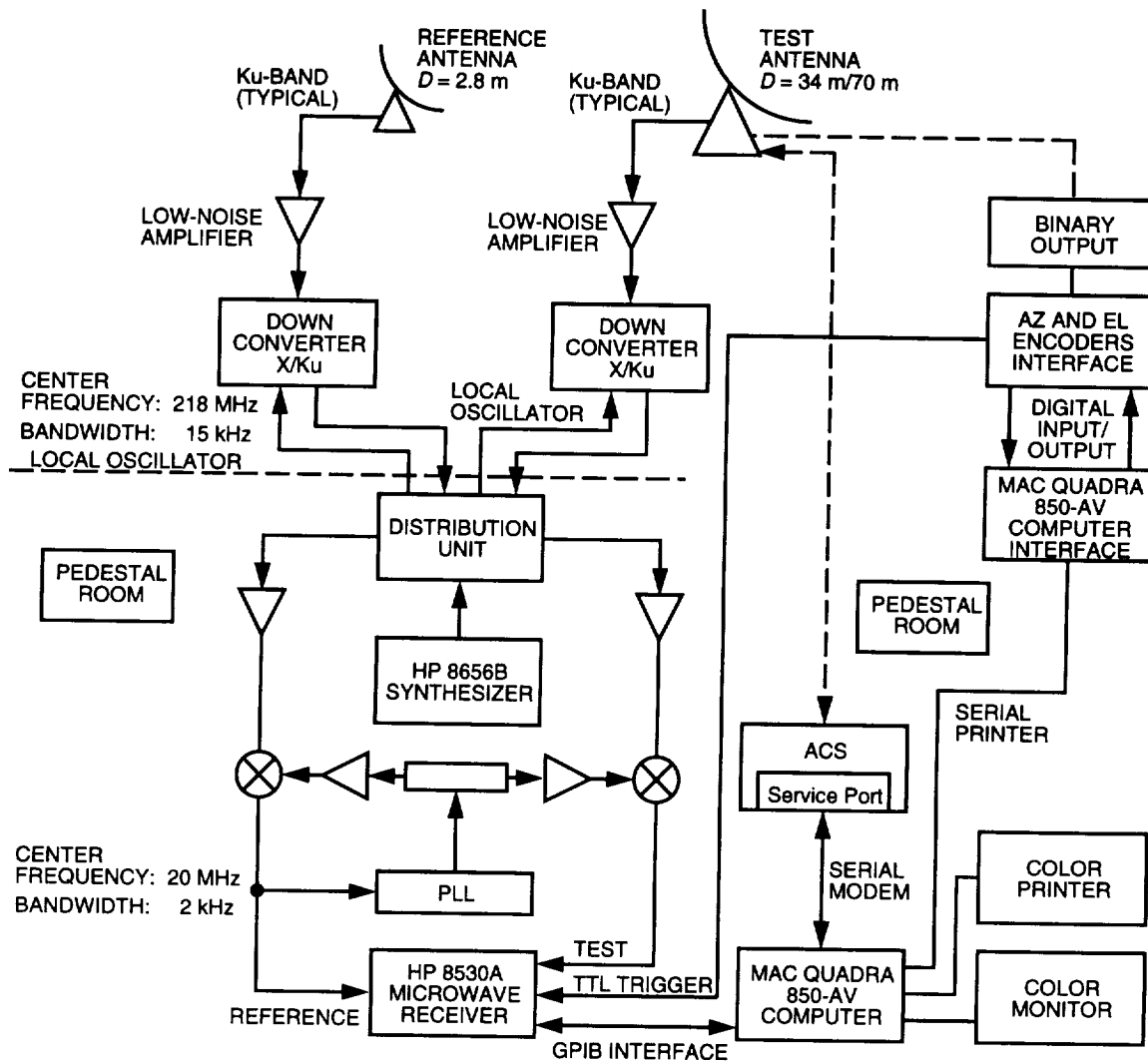
Fig. 1. MAHST block diagram.

precision amplitude and phase measurements of the ground antenna sidelobes with a 90-dB dynamic range. The far-field data are collected by continuously scanning the test antenna against the signal from a geosynchronous satellite, sampling a two-dimensional grid directly on the u, v (direction cosine) space. Each subscan start position is updated in real time to track the predicted orbit position of the geosynchronous satellite. The angular extent of the response that must be recorded is inversely proportional to the size of the required resolution cell in the processed holographic maps. The data processing provided with the system computes the desired information.[1] It is the information in the surface error map that is used to compute the adjustments of the individual panels in an overall main reflector best-fit reference frame. The amplitude map provides valuable information about the energy distribution in the antenna aperture. A short summary of the theory is presented in Appendix A.

---

[1] D. J. Rochblatt, *A User Manual, Data Processing Software for Microwave Antenna Holography: Computer Programs for Diagnostics, Analysis, and Performance Improvement of Large Reflector and Beam Waveguide Antennas,* JPL D-10237 (internal document), Jet Propulsion Laboratory, Pasadena, California, January 15, 1993.

II. Holographic Measurements and Results

The holographic measurements of DSS 24 were conducted during May 13 through 23, 1994 (Table 1). Four high-resolution (33.7-cm), four medium-resolution (84.8-cm), and one low-resolution (172-cm) measurements were performed (for a total of nine). Diagnostics, analysis, subreflector position, and panel setting listing were all derived on site. The antenna panels were reset on May 19, 1994 (excluding panels under the shadow areas of the quadripod). Eight measurements were made at the rigging angle of 46.3 deg, from the antenna Cassegrain focus at f1, utilizing the beacon signal at Ku-band (11.9225 GHz) from the GSTAR-1 satellite. Only one medium-resolution measurement at the low-elevation angle of 12.7 deg (f1 focus) was made due to the short time allocated for the holographic measurements. The beacon signal from the INTELSAT-V (307) satellite at Ku-band (11.7009 GHz) was utilized for the low-elevation measurement.

The data acquisition time for the high-resolution maps required for panel setting was 6.5 h. The data processing for obtaining panel setting information took 8 h. It took an additional 8 h to actually reset the panels of the antenna. The measurement and data processing time required for subreflector position correction for a 34-m antenna is approximately 2 h (two iterations).

Table 1. DSS-24 holographic measurements.

Date	File no.	EL angle, deg	Array size	Remarks
5/13/94	DSN006	46.4	25 × 25	Subreflector correction
5/13/94	DSN007	46.3	51 × 51	Verification
5/14/94	DSN008	46.3	127 × 127	Panel setting derivation
5/16/94	—[a]	—[a]	—[a]	Briefing at JPL
5/17/94	DSN009	46.3	51 × 51	Geometry confirmation
5/18/94	DSN010	46.3	121 × 121	Repeatability verification
5/19/94	—[a]	—[a]	—[a]	Panel setting
5/19/94	DSN011	46.3	51 × 51	After panel setting
5/20/94	DSN012	46.3	127 × 127	After panel setting and touch up
5/22/94	DSN013	46.3	127 × 127	Bad scan
5/23/94	DSN014	12.7	51 × 51	Low-elevation map

[a] No measurement taken.

A. Subreflector Position Correction

Appendix B summarizes the theory of subreflector position correction via holography as applied at DSS 24 (for a 70-m antenna, the processing is slightly different). The subreflector correction is derived from the low-order phase distortions in the antenna aperture function derived from low-resolution (25 × 25 array for a 34-m antenna, or 51 × 51 for a 70-m antenna) holographic imaging. Since the derivation is based on an iteration algorithm, two low-resolution measurements are required. The time required for a single low-resolution measurement is approximately 45 min, and data processing time is 16 min. Figure 2 shows the far-field amplitude pattern of DSS 24 as found in the initial stage of the holographic measurements, and Fig. 3 shows the same information after holographic corrections were applied. The corrections that were derived and applied to the subreflector positioner are 0.516 in. in the −X direction, 0.375 in. in the +Y direction and 0.135 in. in the +Z direction. From observing the far-field patterns in Figs. 2 and 3, it is clear that the antenna went through a transformation from being unfocused to focused. The performance improvement obtained by setting the subreflector is 0.25 dB at X-band and 3.6 dB at Ka-band. The
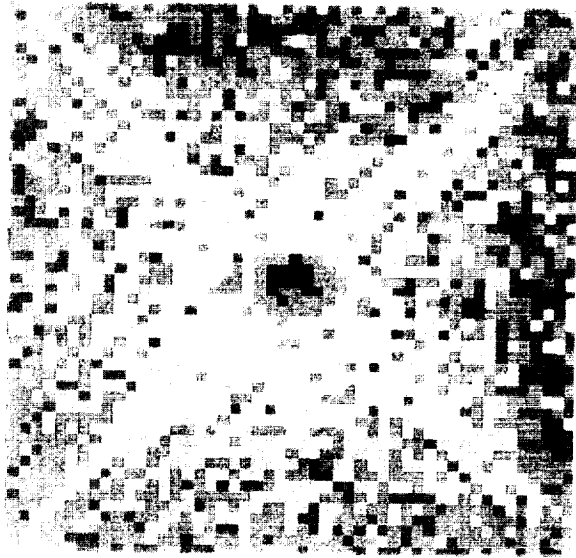
Fig. 2. Far-field pattern recorded on May 13, 1994, indicating an unfocused antenna. (Color image available electronically.)
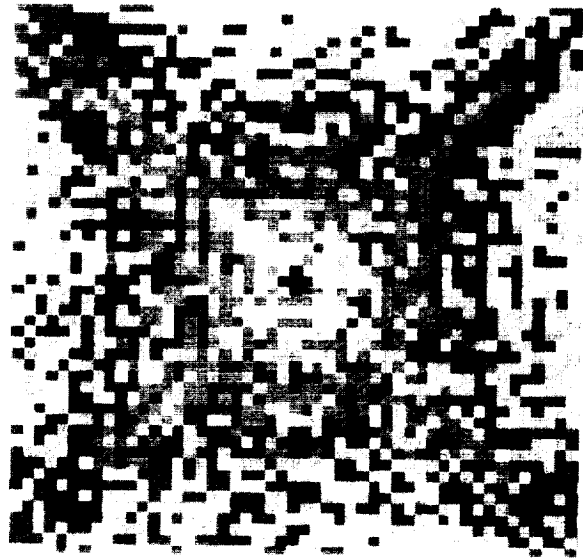

Fig. 3. Far-field pattern recorded on May 14, 1994, after correcting the subreflector position, indicating a focused antenna. (Color image available electronically.)

derivation of the subreflector correction in the X-direction was especially critical since no servo drive but only manual mechanical adjustment is available for this axis (for DSS 24), and therefore the traditional trial-and-error methods are not efficient. Figures 4 and 5 show a one-dimensional elevation cut of the far-field amplitude pattern (11.9225 GHz) before and after corrections, respectively, that were made to the subreflector. Figures 6 and 7 show a one-dimensional azimuth cut of the far-field amplitude pattern (11.9225 GHz) before and after corrections, respectively, that were made to the subreflector.

Holography can derive the subreflector (X, Y, Z) position at any observation angle from which geostationary satellites can be viewed. For the 70-m antennas, two tilt-angle corrections are also included. In practice, usually three elevation angles are readily available from Goldstone (approximately 45-, 37-, and 12-deg elevation). However, it is shown here that when the finite element model for the subreflector offset is accurate (as is the case for DSS 24), adding to it a constant term derived at a single elevation (e.g., 45 deg) creates a new model that is accurate over all elevation angles. Since the time allocated for holographic measurement was minimal, only this derivation was possible. Derivation of the subreflector offsets from the f3 focus position will compensate for any misalignment of the beam-waveguide (BWG) mirrors, and thus may cause peak antenna gain to occur at different elevation angles, and away from the rigging angle for different feed positions.

Equation (1) was derived[2] using a finite element modeling of DSS 24 for the subreflector offsets (X, Y, Z) as a function of the elevation angle (EL):

$$
\left.
\begin{aligned}
X &= 0 \\[2ex]
Y &= -0.008\{\sin(45) - \sin(\text{EL})\} + (-1.485)\{\cos(45) - \cos(\text{EL})\} \\[2ex]
Z &= -0.164\{\sin(45) - \sin(\text{EL})\} + (-0.004)\{\cos(45) - \cos(\text{EL})\}
\end{aligned}
\right\}
\tag{1}
$$

[2] R. Levy, "DSS-24 Subreflector Positioner Offsets," JPL Interoffice Memorandum 3323-94-032 (internal document), Jet Propulsion Laboratory, Pasadena, California, February 16, 1994.
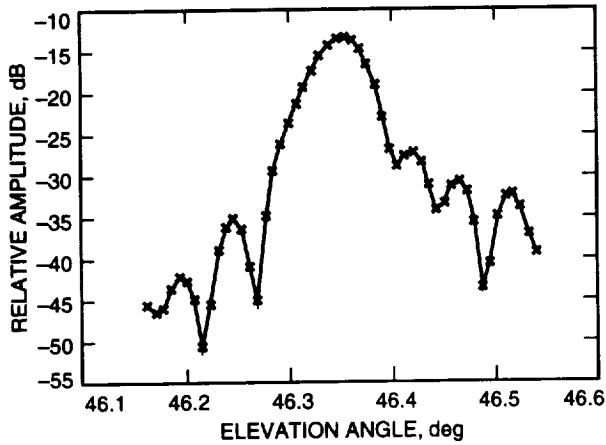
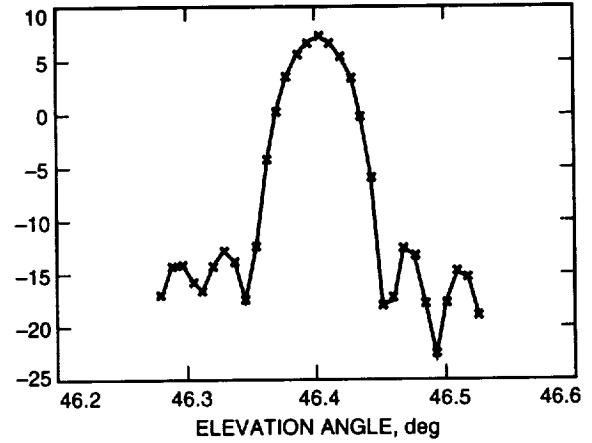**Fig. 4. Far-field elevation cut as found (dB-relative scale).**

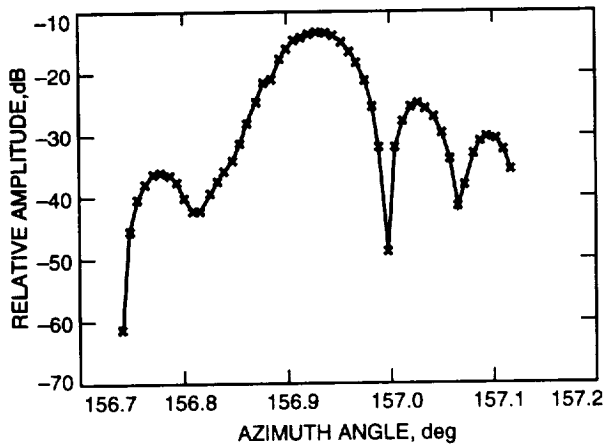**Fig. 5. Far-field elevation cut after holography (dB-relative scale).**

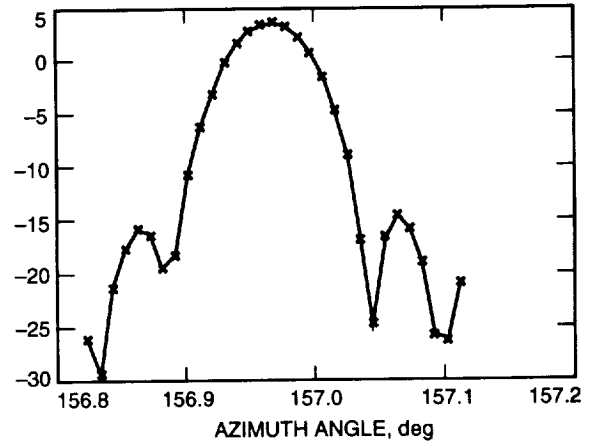**Fig. 6. Far-field azimuth cut as found (dB-relative scale).**

Fig. 7. Far-field azimuth cut after holography (dB-relative scale).

In Eq. (2), a constant term derived by holography at 46.3-deg elevation (and one iteration) is added to Eq. (1):

$$\left.\begin{array}{l} X = -0.516 \\[2mm] Y = 0.375 - 0.008\{\sin(45) - \sin(EL)\} + (-1.485)\{\cos(45) - \cos(EL)\} \\[2mm] Z = 0.135 - 0.164\{\sin(45) - \sin(EL)\} + (-0.004)\{\cos(45) - \cos(EL)\} \end{array}\right\} \qquad (2)$$

Holography and radiometry should derive the same subreflector offsets at approximately 45-deg elevation. (Note that holography did not optimize the subreflector position after panel setting due to time constraints imposed on the project.) Under these conditions, the maximum deviation in the equation for the Z-axis is 0.03 in. at 10-deg elevation, which translates to 0.045 dB at Ka-band. The remaining terms in the equation for the Y-axis deviate by 0.07 in. at 80-deg elevation, which translates to 0.02 dB at Ka-band (Fig. 8).
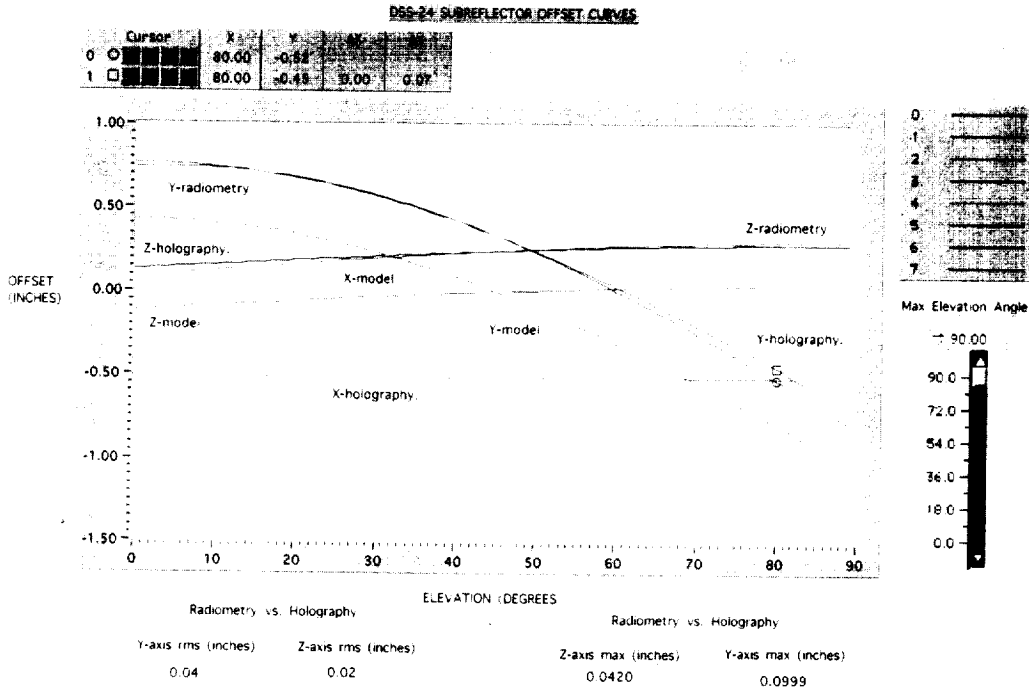
Fig. 8. Subreflector offsets versus elevation angle. (Color image available electronically.)

B. Panel Setting

The theory of panel setting as used at DSS 24 is described in [5]. Figure 9 is the mechanical surface error map of DSS 24 derived from the measurement on May 14, 1994 (DSN008). The normal rms surface error of the inner 32-m diameter at a resolution of 33.7 cm is 0.50 mm. Panel settings were derived from this scan (DSN008) after verifying repeatability (scan DSN010) and confirming coordinate geometry and pixel registering accuracy. Panels 1, 7, 13, and 19 in ring 2 (counting 1 from the center and 9 as the outermost ring) were installed last and can easily be distinguished (they are 90 deg apart). Figure 10 is the mechanical surface error map of DSS 24 derived from the measurement on May 20, 1994 (DSN012) after panel setting. The normal rms surface error of the inner 32-m diameter at a resolution of 33.7 cm is 0.258 mm, and the infinite resolution axial error is 0.25 mm. The precision of DSS 24 (diameter/rms) is 1.36×10^5, the highest of the NASA/JPL DSN antennas. The performance improvements achieved via holography by resetting the DSS-24 surface and positioning the subreflector are 0.35 dB at X-band and 4.9 dB at Ka-band; these improvements are summarized in Table 2. The efficiency of DSS 24 at the nominal elevation angle of 45 deg was increased from 68.83 percent to 74.61 percent at X-band (f3 referenced to horn aperture) and from 19.83 percent to 61.29 percent at Ka-band (f3 referenced to horn aperture). Figure 11 shows the gain loss of DSS 24 due to main reflector surface errors (using the Ruze equation [6]) before and after panel setting. Figure 12 is a plot of DSS-24 gain (from f3) versus frequency, indicating that its gain limit is at 95 GHz. As can be seen from Table 3,[3] the MAHST provided the critical RF performance necessary not only to meet the project requirements and goals, but to surpass them.

Figure 13 is the predicted surface error map of DSS 24 derived from the measurement on May 14, 1994 (DSN008), indicating that an rms surface error of 0.20 mm could have been achieved if the panel

---

[3] The "expected" values in this table were supplied from notes by W. Veruttipong, Ground Antennas and Facilities Engineering Section, and D. A. Bathker, DSN Advanced Planning Office, "DSS-24 RF Optics Design Detailed Gain/Noise Budgets for S/X Ka-Bands," Jet Propulsion Laboratory, Pasadena, California, February 7, 1992.
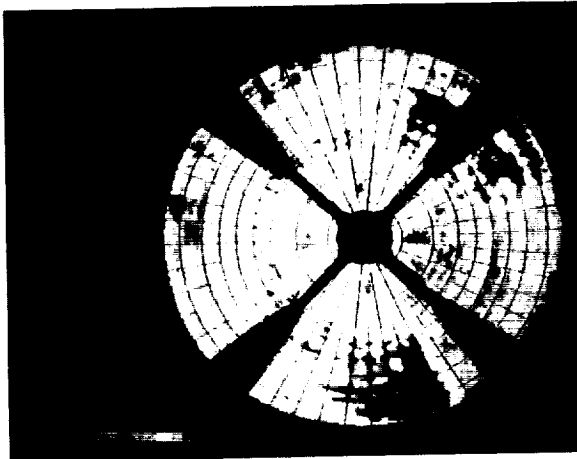
Fig. 9. High-resolution (33.7-cm) error map of the central 32 m of the antenna surface at 46.3-deg elevation, before panel setting, as derived from scan DSN008 (May 14, 1994). The normal, axial, and infinite resolution axial rms errors are 0.50, 0.44, and 0.475 mm, respectively. (Color image available electronically.)
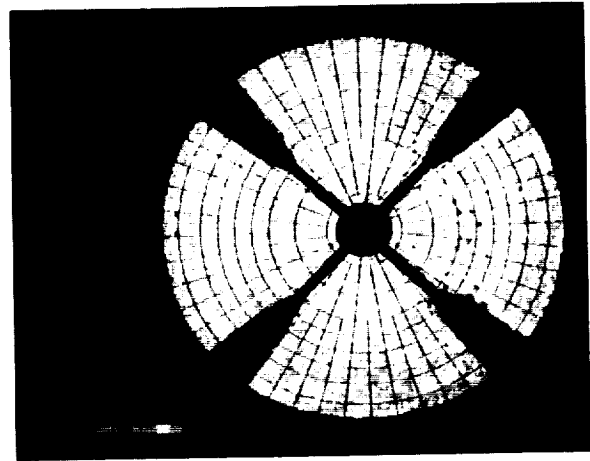

Fig. 10. High-resolution (33.7-cm) error map of the central 32 m of the antenna surface at 46.3-deg elevation, after panel setting, as derived from scan DSN012 (May 20, 1994). The normal, axial, and infinite resolution axial rms errors are 0.26, 0.23, and 0.25 mm, respectively. (Color image available electronically.)

Table 2. Performance improvement by microwave holography at approximately 45-deg elevation.

Frequency, GHz	Panel setting, dB	Subreflector, dB	Total, dB
X-band, 8.45	0.1	0.25	0.35
Ka-band, 32	1.27	3.6	4.87

setting listing were executed precisely (the accuracy of the panel setting listing is 35 μm). DSS 24 has 348 panels and 1716 adjusting screws. The rms surface of the individual panels is 0.127 mm and the rms surface error of the subreflector is 0.125 mm. Since a precision panel adjusting tool was not available, and in order to reduce the panel setting time, the panel listings were rounded to the nearest $\pm 1/8$ of a screw turn (± 0.16 mm). This enabled resetting the entire dish in an 8-h period. The inferred panel setting accuracy is therefore 0.175-mm rms.

Figure 14 is a map differencing (DSN010 – DSN008) that verified repeatability and confirmed coordinate geometry and pixel registering accuracy. Before scan DSN010 was recorded, two panels were intentionally moved as targets. Panel 23 in ring 3 and panel 23 in ring 5 were translated −1.00 mm. In the map differencing of Fig. 14, the two panels appear in the correct location (within the boundaries of the panel masking) and with the correct polarity and within the expected range (the blue color next to the last in Fig. 14 corresponds to −1.07 mm). (Color images are available electronically.)

Figures 15 and 16 are the far-field amplitude and phase functions, respectively. The figures show 127×127 samples to the 51st sidelobe, recorded on May 20, 1994, after panel setting. The samples are separated by 34 mdeg (in the u, v space), forming a window of ± 2.14 deg relative to the antenna main beam at Ku-band. The far-field amplitude (Fig. 15) shows a well-concentrated and symmetrical pattern, and the far-field phase (Fig. 16) shows a symmetrical pattern with well-concentric rings as expected. Figure 17 is the derived DSS-24 aperture amplitude function, indicating a well-uniform illuminating antenna, while the energy rolls off −15 dB just over the edge of the antenna (the last 2 m of the diameter).
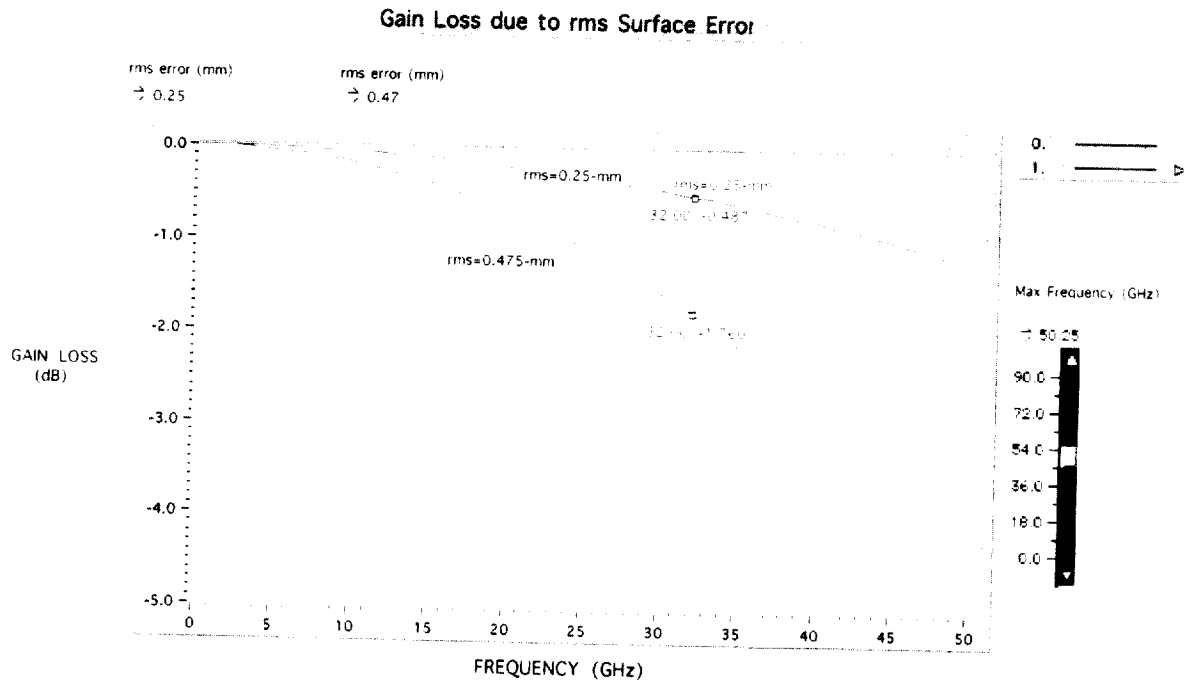
Gain Loss due to rms Surface Error

Fig. 11. Gain loss due to main reflector surface error (based on [6]). (Color image available electronically.)
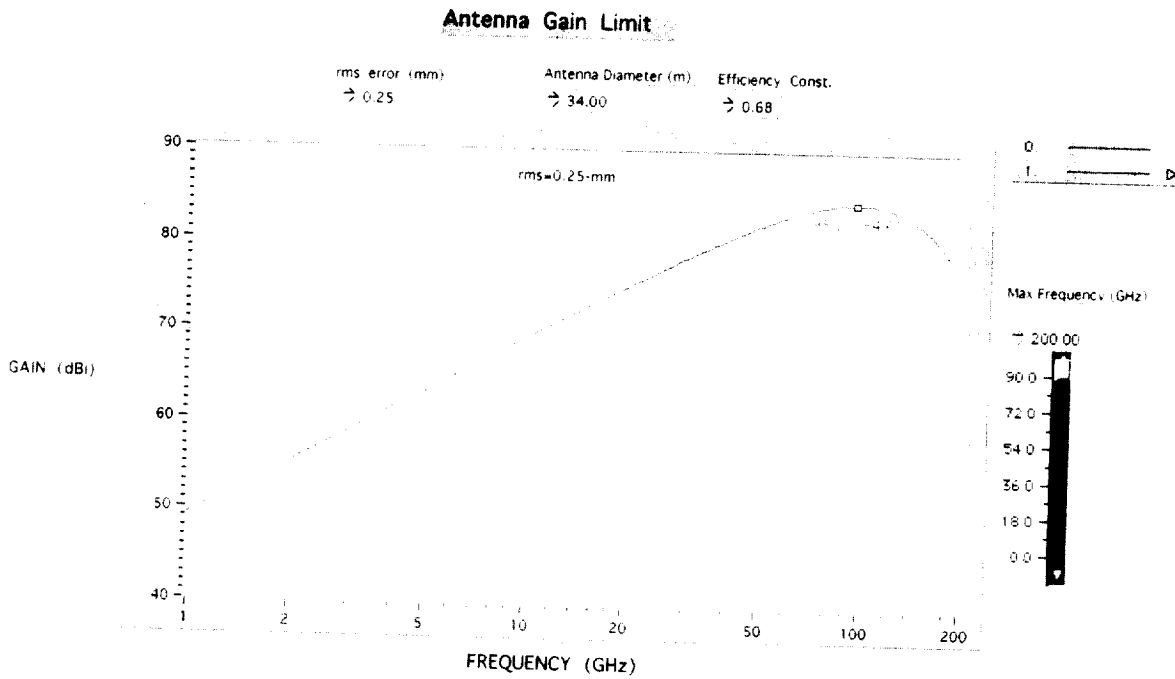
Antenna Gain Limit

Fig. 12. Gain versus frequency. (Color image available electronically.)

Table 3. Maximum aperture efficiency at rigging elevation angles referenced to horn aperture.

Parameter	Percent aperture efficiency at X-band		Percent aperture efficiency at Ka-band	
	f1[a]	f3[b]	f1[c]	f1[d]
Expected[e]	78.9 ± 1.5	77.6 ± 2.5	68.2 ± 3.0	59.9 ± 4.0
Specified	—[f]	72.0	—[f]	41.0
As built	71.2 ± 3.0	68.83 ± 3.0	21.07 ± 4.0	19.83 ± 4.0
Measured post-holography	77.2 ± 2.0	74.61 ± 2.0	65.14 ± 2.3	61.29 ± 2.7

[a] 42.2 deg.

[b] 51.5 deg.

[c] 44.5 deg.

[d] 40.8 deg.
(These elevation angles were supplied by L. S. Alvarez, "Aperture Efficiency Measurements," *DSS-24 Antenna RF Performance Measurements*, JPL D-12277 (internal document), Jet Propulsion Laboratory, Pasadena, California, February 1, 1995.)

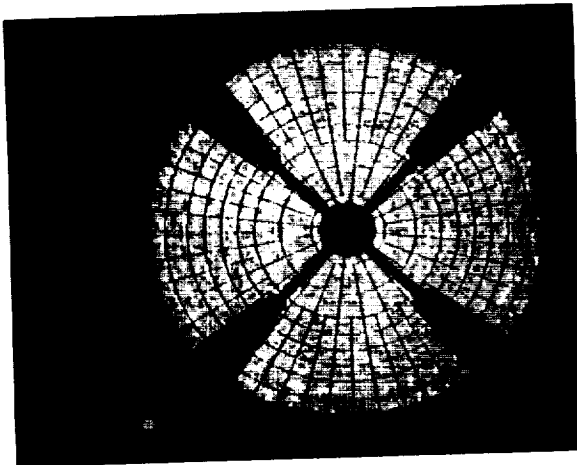[e] W. Veruttipong and D. A. Bathker, op cit.

[f] Not specified.

Fig. 13. Predicted surface error, map derived from DSN008. (Note: This represents the best achievable rigging angle surface that would have resulted if the 1716 screws were adjusted precisely as specified by the software.) (Color image available electronically.)
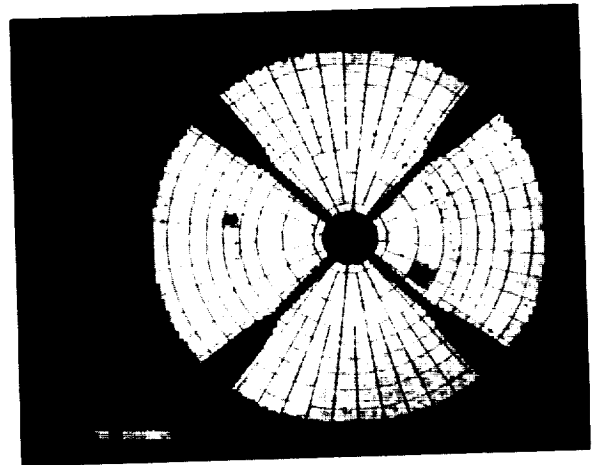
Fig. 14. Map differencing (DSN010 – DSN008) that verified repeatability and confirmed coordinate geometry and pixel registering accuracy. Before scan DSN010 was recorded, two panels were intentionally moved as targets. Panel 23 in ring 3 and panel 23 in ring 5 were translated ≡ 1.00 mm. (Color image available electronically.)

C. Gravity Deformation

Only one medium-resolution (84.8-cm) holographic measurement was recorded at a low elevation angle of 12.5 deg (Table 1). The normal rms surface error of 0.39 mm was computed at a resolution of 84.8 cm and is presented in Fig. 18. The systematic component of the antenna deformation was derived by fitting the data to a set of radial and circumferential polynomials (modified Jacobi polynomials [7], which are similar to Zernike polynomials, which are more common in optics). The first 18 terms of the modified Jacobi polynomial are tabulated in Table 4 and are shown in Fig. 19, indicating an rms surface error of 0.29 mm. A slight structural "twist" at the low elevation angle of 12.5 deg is noticed in the result. The low-order gravity deformation of DSS 24 is predominately astigmatic (80.3 percent), and its symmetrical
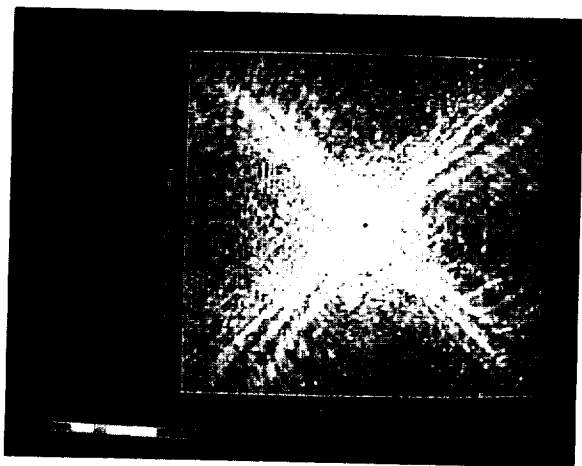
Fig. 15. Far-field (DSN012) amplitude pattern after panel setting. (Color image available electronically.)
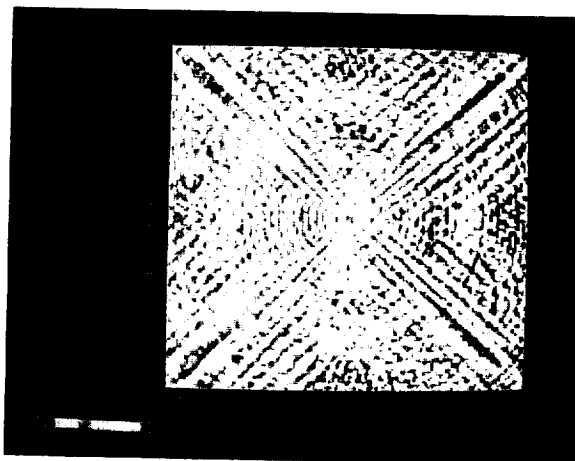

Fig. 16. Far-field (DSN012) phase pattern after panel setting. (Color image available electronically.)
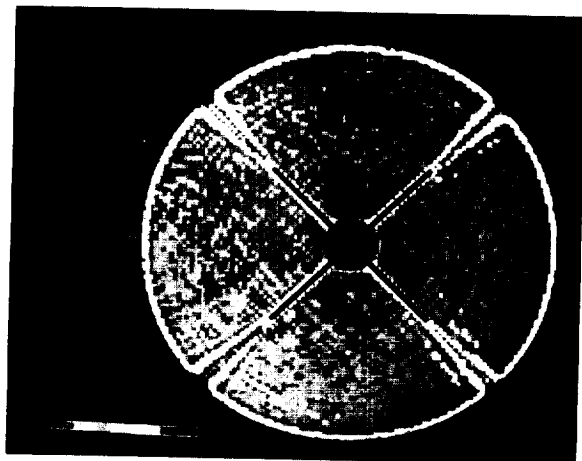

Fig. 17. Derived antenna aperture amplitude illumination (DSN008). (Color image available electronically.)
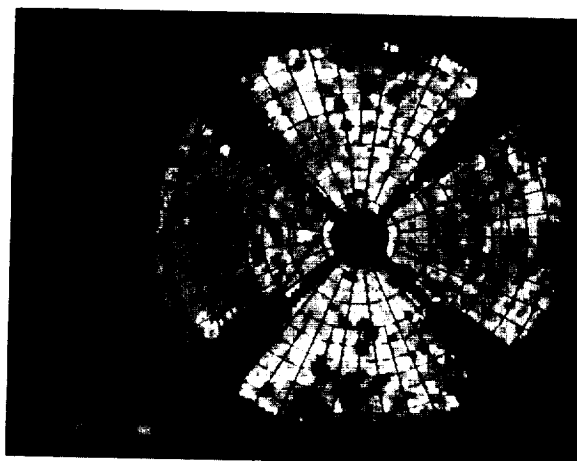

Fig. 18. Medium-resolution (84.8-cm) error map of the central 32 m of the antenna surface at 12.5-deg elevation after panel setting, derived from scan DSN014 (May 23, 1994). The normal rms error is 0.39 mm. (Color image available electronically.)

(top–down/left–right) component is shown in Fig. 20 with an rms error of 0.26 mm. Figure 21 is the map-differencing of Fig. 19 from Fig. 18, indicating that the remaining gravity distortion components of the antenna structure are of higher order or "random." The root sum squares (rss) of the systematic component and the random component agree well with the total distortion. The predicted gain loss at angles 33.8 deg away from the rigging angle is estimated at −0.046 dB at X-band and −0.65 dB at Ka-band. Efficiency measurements at X-band and Ka-band from the f3 focus indicate a gain loss of −0.042 dB and −0.575 dB at 33.8 deg from a peak gain at 51.43 deg and 40.8 deg, respectively, agreeing well with the holography predictions.

The gravity performance of DSS 24 was greatly improved relative to the gravity performance of DSS 13. It was characterized and analyzed by holography:[4] gravity distortion of DSS 13 causes 2.27-dB gain loss at 32 GHz at 33.8 deg from the rigging angle.

---

[4] D. J. Rochblatt and B. L. Seidel, Holographic Measurements of DSS-13 Beam Waveguide Antenna, December 2, 1991 Through February 6, 1992, JPL D-9910 (internal document), Jet Propulsion Laboratory, Pasadena, California, July 15, 1992.
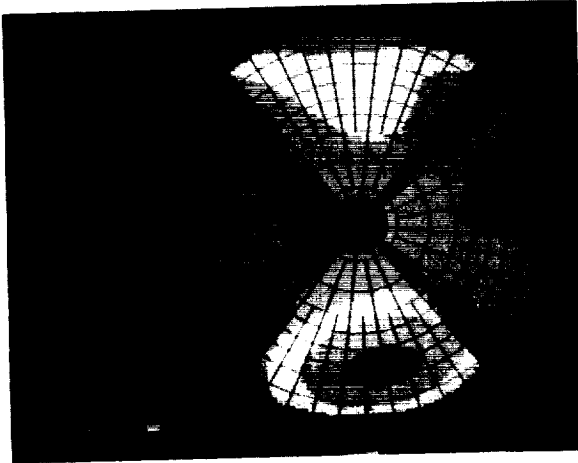
Fig. 19. Systematic component of the low-elevation error map represented by the first 18 terms of the modified Jacobi polynomials. The normal rms surface is 0.29 mm. (Color image available electronically.)
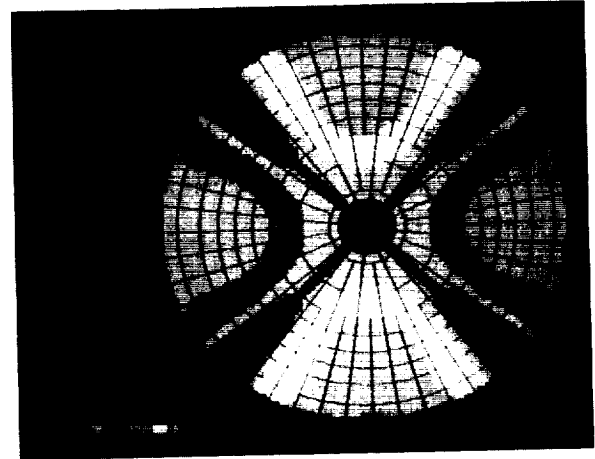

Fig. 20. Astigmatic component of the gravity distortion represents 80.3 percent of the total systematic distortion due to gravity. The normal rms surface is 0.26 mm. (Color image available electronically.)
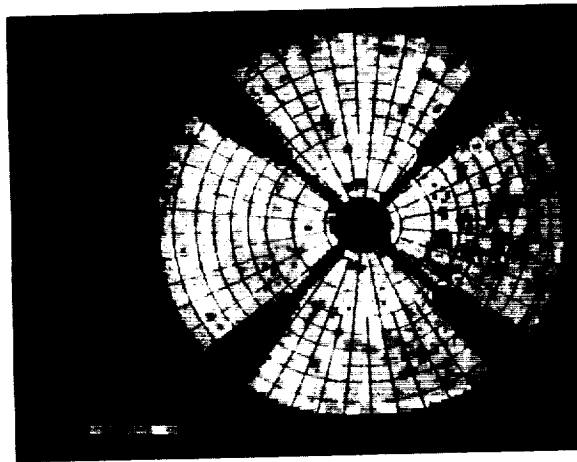
Fig. 21. Random component surface at 12.5-deg elevation. The normal rms surface error is 0.27 mm. (Color image available electronically.)

Table 4. Modified Jacobi polynomial decomposition for gravity deformation characterization.

n	m	C, in.	D, in.
0	0	-0.006389	0.000000
0	1	-0.000450	0.000000
0	2	-0.001264	0.000000
1	0	0.001766	0.00243
1	1	0.001961	-0.003240
1	2	0.000329	0.001786
2	0	-0.009939	0.000196
2	1	-0.002407	-0.001486
2	2	-0.001709	0.000767

III. Conclusions and Recommendations

The JPL MAHST provided DSS 24 with the critical RF performance necessary not only to meet the project requirements and goals, but to surpass them, transforming DSS 24 to the highest precision antenna in the DSN. The main reflector panels were set to 0.25-mm rms and the subreflector was positioned in its focus location as seen from f1 at 46.3-deg elevation. New offset curves were derived for the subreflector position at all elevation angles as seen from f1. Unfortunately, time was not allocated for holographic measurements from the f3 focus.

It is recommended that in future holographic metrology of newly built DSN BWG antennas, time for the following measurements be provided:

(1) Low resolution at Ku-band (12 GHz) from f1 rigging angle ($\approx$45.0 deg) to set the subreflector position.

(2) High resolution at Ku-band from f1 rigging angle to set the panels.

(3) Low resolution at Ku-band from f1 at approximately 37-deg elevation to set the subreflector.

(4) Low resolution at Ku-band from f1 low elevation ($\approx$12 deg) to set the subreflector.

(5) High resolution at Ku-band from f1 low elevation to image the surface and derive high-resolution gravity deformation maps.

(6) Medium resolution at Ku-band from the f3 rigging angle to diagnose misalignments in the BWG mirrors and characterize the BWG effects.

(7) Medium resolution at Ku-band from the f3 low elevation angle to diagnose misalignments in the BWG mirrors and their effect on performance.

(8) Medium resolution at X-band (7.7 GHz) to diagnose misalignments in the BWG mirrors and detect any problems (moding) in the feed.

Acknowledgments

References

[1] D. J. Rochblatt, "Microwave Antenna Holography System," *Proceedings of Technology 2004 Conference, Test and Measurements Part 1*, Washington, DC, November 8–10, 1994.

[2] D. J. Rochblatt, "Microwave Holography of DSN Reflector Antennas," *Proceedings of the 1994 AMTA Workshop, Modern Imaging and Diagnostic Technique for RCS and Antennas,* University of Washington, Seattle, Washington, June 24, 1994.

[3] D. J. Rochblatt, "Microwave Holography Helps Improve Performance of Large Antennas," *LASER Tech Briefs,* Publication of NASA Tech Briefs, vol. 1, no. 1, p. 81, September 1993.

[4] D. J. Rochblatt and B. L. Seidel, "Microwave Antenna Holography," *IEEE Trans. Microwave Theory and Techniques, Special Issue on Microwaves in Space,* vol. 40, no. 6, pp. 1294–1300, June 1992.

[5] D. J. Rochblatt, "A Microwave Holography Methodology for Diagnostics and Performance Improvement for Large Reflector Antennas," *The Telecommunications and Data Acquisition Progress Report 42-108, October–December 1991,* Jet Propulsion Laboratory, Pasadena, California, pp. 235–252, February 15, 1992.

[6] J. Ruze, "Antenna Tolerance Theory—A Review," *Proc. IEEE,* vol. 54, pp. 663–640, April 1966.

[7] V. Galindo-Israel and R. Mittra, "A New Series Representation for the Radiation Integral with Application to Reflector Antennas," *IEEE Trans. AP,* vol. AP-25, pp. 631–635, September 1977 (Correction, *IEEE Trans. AP,* vol. AP-26, p. 628, July 1978).

[8] D. J. Rochblatt and Y. Rahmat-Samii, "Effects of Measurement Errors on Microwave Antenna Holography," *IEEE Trans. Antennas Propagat.,* vol. 39, no. 7, pp. 933–942, July 1991.

Appendix A

Theory

The mathematical relationship between an antenna far-field pattern (T) and the antenna-induced surface current distribution (J) is given by the exact radiation integral relationship (Fig. A-1):[5]

$$\vec{T}(u,v) = \int\int_s \vec{J}(x',y') \exp^{jkz'} \left[\exp^{-jkz'(1-\cos\theta)} \right] \exp^{jk(ux'+vy')} dx'dy' \qquad \text{(A-1)}$$

where $Z'(x',y')$ defines the surface $S, (u,v)$ is the direction cosine space, and θ is the observation angle. For a small angular extent of the far-field pattern, this expression reduces to

$$\vec{T}(u,v) = \int\int_s \vec{J}(x',y') \exp^{jkz'} \exp^{-jk(ux'+vy')} dx'dy' \qquad \text{(A-2)}$$
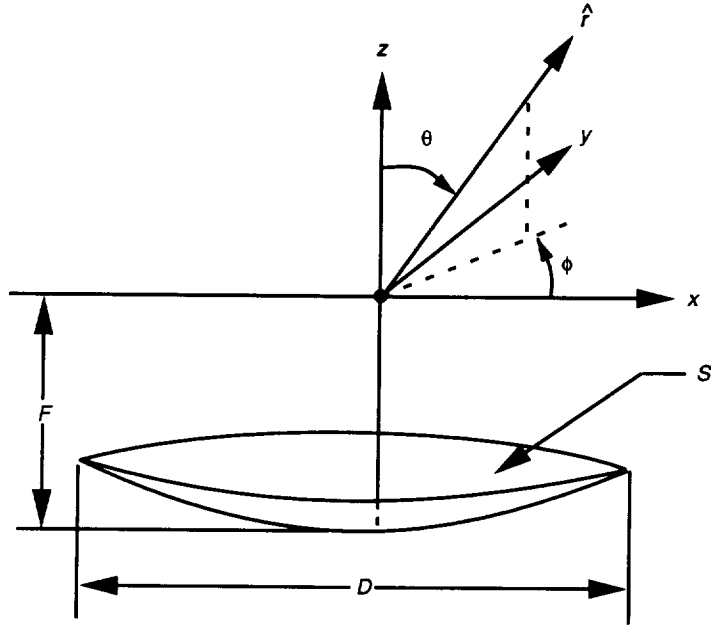
---

[5] D. J. Rochblatt, op cit.

Fig. A-1. Antenna geometry.

Equation (A-2) is an exact Fourier transform of the induced surface current. To derive the residual surface error, geometrical optics ray tracing is used to relate the normal error ε to the axial error and phase in a main reflector paraboloid geometry (Fig. A-2).

$$\frac{1}{2}\Delta PL = \frac{1}{2}[P'P + PQ] = \frac{1}{2}\left[\frac{\varepsilon}{\cos\varphi} + \frac{\varepsilon\cos 2\varphi}{\cos\varphi}\right] = \varepsilon\cos\varphi \qquad \text{(A-3)}$$

$$\text{Phase}(\Delta PL) = \frac{4\pi}{\lambda}\varepsilon\cos\varphi \qquad \text{(A-4)}$$

and for a paraboloid,

$$\cos\varphi = \frac{1}{\sqrt{1 + \dfrac{x^2 + y^2}{4F^2}}} \qquad \text{(A-5)}$$

where F is the antenna focal length.

Allowing for the removal of a constant phase term and substituting Eq. (A-4) into Eq. (A-2),

$$\vec{T}(u,v) = \exp^{-j2kF}\int\int_s\left[\left|\vec{J}(x',y')\right|\exp^{j4\pi\frac{\varepsilon}{\lambda}\cos\varphi}\right]\exp^{jk(ux'+vy')}\,dx'dy' \qquad \text{(A-6)}$$

For processing sampled data, the associated discrete Fourier transform (DFT) is utilized:
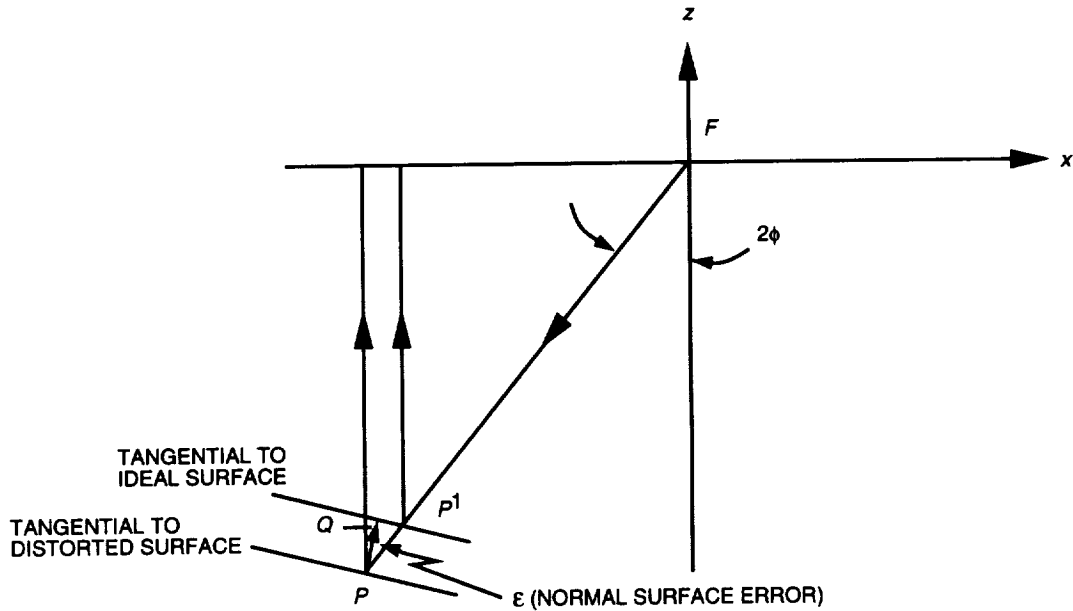
Fig. A-2. Surface distortion geometry.

$$T(p\Delta u,\ q\Delta v) = sxsy \sum_{n=-N1/2}^{N1/2-1} \sum_{m=-N2/2}^{N2/2-1} J(nsx, msy)\, \exp^{j2\pi((np/N1)+(mq/N2))} \qquad (A\text{-}7)$$

where $N1 \times N2$ is the measured data array size; sx and sy are the sampling intervals in the aperture coordinates; $n, m, p,$ and q are the integers indexing the discrete samples; and Δu and Δv are the sampling intervals in u, v far-field space. Since the magnitude of the far-field pattern is essentially bounded, the fast Fourier transform (FFT) is usually used for computation. The solution for the antenna residual surface error in the normal direction is, therefore,

$$\varepsilon(x,y) = \frac{\lambda}{4\pi} \sqrt{1 + \frac{x^2 + y^2}{4F^2}}\, \mathrm{Phase}\left[\exp^{j2kF}(FFT)^{-1}[T(u,v)]\right] \qquad (A\text{-}8)$$

The spatial resolution in the final holographic map δ is defined here at the -3-dB width of the convolving function [4]:

$$\delta = \frac{D}{kN} \qquad (A\text{-}9)$$

where D is the main reflector diameter, N is the square root of the total number of data points, and k is the sampling factor, usually $0.5 < k < 1.0$. The lateral resolution is inversely proportional to the number of sidelobes measured. For a 34-m-diameter antenna, for example, a resolution of 0.337 m in the final holographic map can be achieved with a data array size of 127×127 (16,129) and sampling factor of 0.794. For a 34-m antenna constructed of 348 panels, this measurement will enable imaging of each panel by 33 resolution cells. In Figs. 15 and 16, the far-field amplitude and phase are measured on rectangular coordinates of 127×127 with sampling intervals of 34.0 mdeg (the sampling factor is 0.80).

C-4.

Figures 17 and 10 show the aperture amplitude and surface error function, respectively, with a lateral resolution of 0.337 m.

The accuracy in each resolution cell of the final holographic map is [8]

$$\sigma = 0.082 \frac{\lambda D}{\delta SNR} \tag{A-10}$$

where λ is the wavelength, SNR is the beam peak voltage signal-to-noise ratio, and σ is the standard deviation (accuracy) in recovering the mean position of a resolution cell. The accuracy across holographic maps varies with the antenna aperture amplitude taper illumination. Results are better at the center of the dish and gradually become worse toward the edge of the dish. For a uniformly illuminated dish, accuracy stays relatively constant through most of the dish and becomes quickly worse just at the edge where the illumination falls off rapidly. Note in Eq. (A-10) that the accuracy is inversely proportional to the spatial resolution of Eq. (A-9) due to the larger averaging area available at the larger resolution cell. For a holographic measurement receiver incorporating a multiplier integrator or a divider integrator (for example, HP8530A), the effective signal-to-noise ratio SNR_e can be expressed as [8]

$$SNR_e \left[\sqrt{\frac{1}{SNR_t^2} + \frac{1}{SNR_r^2} + \frac{1}{SNR_t^2 SNR_r^2}} \right]^{-1} \tag{A-11}$$

where SNR_t is the test channel SNR and SNR_r is the reference channel SNR.

Phase errors introduced during the measurement due to pointing and subreflector position errors are removed via a best-fit paraboloid program. The best-fit paraboloid is found by least-squares fitting the data (residual surface error function), allowing 6 degrees of freedom in the model [3].[6] This algorithm ensures that the minimum adjustment (distance) is computed for the screw adjusters. The least-squares fit is computed by minimizing S, the sum of the squares of the residual path-length changes:

$$S = \sum_{i=1}^{N^2} \Gamma(\Delta PL_i)^2 A_i \tag{A-12}$$

where A_i is the amplitude weighing factor associated with the ith data point, Γ is the masking operation that is antenna-type dependent, and ΔPL_i is the path-length change at point (x_i, y_i, z_i). It is correct to apply the best-fit paraboloid algorithm to either the conventional Cassegrain paraboloid-hyperboloid or dual-shaped reflector systems, even though the latter does not use a paraboloid as the main reflector. Both of the reflector antenna designs are, overall, plane-wave-to-point source transformers, differing only in their intensity field distribution.

The resultant aperture function at the end of this process is defined here as the effective map,[7] since it includes all phase effects that are contributing to the antenna performance. These frequency-dependent effects include the subreflector scattered feed phase function and strut diffraction effects. Removal of the frequency-dependent effects results in a mechanical map.[8] By deriving panel adjustments based on the effective map, the surface shape will conjugate the phase errors, optimizing the performance of the antenna at a single frequency while degrading the performance of the antenna at all other frequencies.

---

[6] Ibid.

[7] Ibid.

[8] Ibid.

For antennas operating at a single frequency, this procedure is advantageous. However, many antennas operate at several different frequencies and require a wide bandwidth performance response. For these antennas, the mechanical map must be used to derive panel-setting information.

From the mechanical map, surface tolerance efficiency can be computed at frequencies other than the measured frequency by scaling the residual aperture phase errors (which are now due only to surface deviations) to other frequencies [5]:

$$(K)_{surface} = 20 \times \log_{10}$$

$$\times \frac{\sqrt{\left[\sum_{i=1}^{N^2} 10^{ampdb_i/20} \cos\left(\phi_{m_i}\left(\frac{\lambda_m}{\lambda_k}\right)\right)^2\right] + \left[\sum_{i=1}^{N^2} 10^{ampdb_i/20} \sin\left(\phi_{m_i}\left(\frac{\lambda_m}{\lambda_k}\right)\right)\right]^2}}{\sum_{i=1}^{N^2} 10^{ampdb_i/20}}$$

(A-13)

In this computation, it is assumed that the aperture amplitude illumination is frequency independent. The error introduced in this assumption is thus negligible.

To simplify the discussion on panel settings, the normal component of the residual surface error (E_n) is comprised of two parts in this model. One is due to panel misalignment or rigid body motion, and the second is due to surface error resulting from panel bending:[9]

$$E_n = E_b + E_p \tag{A-14}$$

where E_n is the total surface normal error, E_b is the normal error due to panel bending, and E_p is the normal error due to panel misalignment.

To improve the antenna surface error due to panel misalignment, panels are allowed to move as rigid bodies, with 3 degrees of freedom. The panel position correction is computed by least-squares fit. The derived motion of the panel is then used to compute the needed adjustment at the exact location of each screw on the panel. Only the pixels (resolution-cell data) projected on the panel are considered in the computation, with the center of the pixel taken as the criterion of its location. This criterion provides some averaging near the panel edges, flaring it somewhat with its neighbors. In the panel rigid motion algorithms, 3 degrees of freedom are allowed: a translation (Eq. (A-5)) at a reference point and two rotations (tilts) about the radial and circumferential axis (α and β). Screw adjustments at point qi are computed via

$$E_{p_{q_i}} = -(S + d_i \times \tan(\alpha) - (e_i/\cos(\gamma)) \times \tan(\beta)) \tag{A-15}$$

where

$$\gamma = \arctan\left(\frac{R_{Q_k}}{2}F\right) \tag{A-16}$$

and F is the focal length of the best-fit paraboloid and R_{Q_k} is the radial distance from dish center to panel coordinate center.

---

[9] Ibid.

Appendix B

Subreflector Position Correction Via Holography

Subreflector position correction is derived from the low-order phase distortion in the antenna aperture function. The antenna aperture function in holography is derived from the measured far-field complex (amplitude and phase) function. Zernike or modified Jacobi polynomial and global parameter fit can all be applied.[10] The global best-fit paraboloid is found by permitting 6 degrees of freedom in the model: three vertex translations (X_0, Y_0, Z_0), two rotations (α, β), and a focal length (F) change (K).

The least-squares fit problem is solved by minimizing the sum squares of the residual path-length error:

$$S = \sum_{i=1}^{N^2} \Gamma_{(DSS\ 24)}(\Delta PL_i)^2 A_i \tag{B-1}$$

where $\Gamma_{(DSS\ 24)}$ is the masking operator for DSS 24, ΔPL_i is the path-length change, and A_i is the amplitude weighing. The minimum for S is found by solving the six partial differential equations simultaneously:

$$\left.\begin{aligned}
\frac{\partial S}{\partial X_0} &= 2\sum_{i=1}^{N^2} \Gamma_{(DSS\ 24)}\frac{\partial \Delta PL_i}{\partial X_0}\Delta PL_i A_i = 0 \\[2ex]
\frac{\partial S}{\partial Y_0} &= 2\sum_{i=1}^{N^2} \Gamma_{(DSS\ 24)}\frac{\partial \Delta PL_i}{\partial Y_0}\Delta PL_i A_i = 0 \\[2ex]
\frac{\partial S}{\partial Z_0} &= 2\sum_{i=1}^{N^2} \Gamma_{(DSS\ 24)}\frac{\partial \Delta PL_i}{\partial Z_0}\Delta PL_i A_i = 0 \\[2ex]
\frac{\partial S}{\partial \alpha} &= 2\sum_{i=1}^{N^2} \Gamma_{(DSS\ 24)}\frac{\partial \Delta PL_i}{\partial \alpha}\Delta PL_i A_i = 0 \\[2ex]
\frac{\partial S}{\partial \beta} &= 2\sum_{i=1}^{N^2} \Gamma_{(DSS\ 24)}\frac{\partial \Delta PL_i}{\partial \beta}\Delta PL_i A_i = 0 \\[2ex]
\frac{\partial S}{\partial K} &= 2\sum_{i=1}^{N^2} \Gamma_{(DSS\ 24)}\frac{\partial \Delta PL_i}{\partial K}\Delta PL_i A_i = 0 \\[2ex]
K &= \frac{1}{4}\left(\frac{1}{F} - \frac{1}{F'}\right)
\end{aligned}\right\} \tag{B-2}$$

---

[10] Ibid.

After removing systematic pointing errors, the parameters are used to compute the subreflector position error:

$$
\left.
\begin{aligned}
\Delta X &= X_0 - F \sin(\beta) \\[2mm]
\Delta Y &= Y_0 - F \sin(\alpha) \\[2mm]
\Delta Z &= [Z_0 + F\{\cos(\alpha) + \cos(\beta)\} - 2F]
\end{aligned}
\right\}
\qquad \text{(B-3)}
$$